Optimization of PGNAA device and algorithm for testing basicity index of sinter mixture

Long Zhao[1,2] · Xu Xu[1] · Jing-Bin Lu[1] · Ya-Lin Gong[2] · Qing-Feng Song[2] · Qing-Min Shang[2] · Wei Zhang[2] · De-You Yin[2] · Yan-Feng Li[2]

Abstract Sinter is the main raw material in the blast furnace iron-making process, and basicity (CaO/SiO_2) is an important quality index of sinter. Prompt gamma neutron activation analysis is a multi-elemental online detection technology that has been successfully applied in cement, coal, etc. Compared with cement as a raw material, sinter exhibits poor moderation ability and a large neutron absorption cross section. Therefore, cement detection devices are not suitable for sinter mixture detection. In this study, a prompt gamma neutron activation analysis equipment used for testing cement was re-optimized to render it suitable for measuring a sinter mixture. Using Monte Carlo simulation, the comprehensive detection efficiency of the detection device improved by 71.52%. Because of the gamma-ray self-shielding effect of the sinter mixture, the detection errors of CaO and SiO_2 are significant. By applying the gamma-ray self-shielding correction algorithm, the detection accuracies improved, and their linear correlation coefficients R^2 exceeded 0.99. Furthermore, by applying an improved analyzer to a sintering plant, the first-grade product rate of the factory increased by 4.64%.

Keywords Prompt gamma neutron activation analysis · Sinter · Basicity · Monte Carlo simulation

✉ Jing-Bin Lu
  ljb@jlu.edu.cn

1 College of Physics, Jilin University, Changchun 130012, China

2 Dandong Dongfang Measurement and Control Technology Co., Ltd, Dandong 118002, China

1 Introduction

Prompt gamma neutron activation analysis is a rapid and noncontact multi-elemental analysis technique that has been widely used for elemental detection and analysis in various fields, such as cement, coal, and mineral resource industries [1–11]. The prompt gamma neutron activation analysis (PGNAA) technique is based on the detection of prompt gamma rays emitted through thermal neutron capture (n_{th}, γ) or neutron inelastic scattering (n, n′ γ). It can distinguish the elemental categories in the material from the characteristic gamma-ray energy spectrum as well as estimate the elemental content from the intensities of characteristic energy peaks in the spectrum. The short response time of PGNAA renders it appropriate for online process control tasks, such as online quality control in cement factories. Because neutrons have a strong penetrating ability, PGNAA technology can realize the full-section detection of the conveyor belt, and the measurement results can reflect the overall situation. The neutron capture reaction emits gamma rays of high energy, and its detection results are not affected by environmental dust, steam, or other factors. This technology is suitable for industrial production lines with extremely poor environmental conditions.

Sinter is the main raw material in the blast furnace (BF) iron-making process, and basicity (CaO/SiO_2) is an

important quality index of sinter [12]. The fluctuation of basicity significantly affects the BF smooth operation. Every 10% reduction in basicity fluctuation results in an increase in production by 1.5% and coke reduction by 1% in BF. Currently, the control process of sintering production is lagging severely. The control lag is approximately 5 h, which results in a significant fluctuation in the basicity index of the sinter. Hence, real-time and accurate detection of the basicity is crucial to improve the sintering process and sinter quality. In this study, PGNAA analyzer model DF-5701, which was custom designed for the cement industry, was re-optimized to realize real-time online basicity detection. Because of the difference in chemical composition and physical parameters between the sinter mixture and cement raw material, the thermal neutron flux in the sinter mixture was only 62.58% of that in the cement raw material; therefore, the detection device must be optimized and upgraded. Using the Monte Carlo method for the optimization calculation, the comprehensive detection efficiency of the detection device increased by 71.52%. Gamma-ray self-absorption was observed in the sinter mixture, which contributed negatively to the detection results. In this study, the energy spectrum was restored by measuring the degree of gamma-ray self-absorption to improve the detection accuracy of CaO and SiO_2. The linear correlation coefficient R^2 of the calibration samples of CaO and SiO_2 improved from 0.962 and 0.970 to 0.995 and 0.994, respectively. Finally, the upgraded analyzer was applied to the sintering plant. After applying the analyzer, the basicity stability rate of the plant increased by 3.98%, and the first-class product rate of the sinter increased by 4.96%.

2 Instrumentation and methods

In neutron-induced gamma techniques, the characteristic gamma-ray spectrum exhibits the following relationship with the neutron flux [13]:

$$I_{E_i} = \sum w_j \left(\frac{N_A \theta_j}{m_j} \right) \sigma_j \varphi t l_j \varepsilon \quad (1\,\mathrm{MeV} \le E_i \le 10\,\mathrm{MeV})$$
$$j = \mathrm{Ca, Si, O, Mg, Cl, Fe, H, C} \ldots, \tag{1}$$

where I_{E_i} is the gamma-ray count with energy E_i, N_A the Avogadro constant, θ_j the isotopic abundance of element j, w_j the weight percent of element j, m_j the atomic mass of element j, σ_j the neutron capture cross section of element j, φ the neutron flux, t the measurement duration, l_j the gamma-ray abundance per neutron reaction of element j, and ε the detection efficiency.

Any unknown sample spectrum is the sum of the products of the elemental amount and the library spectrum of each element for every pulse-height channel [14].

$$I_{E_i} = \sum B_j A_j \quad (1\,\mathrm{MeV} \le E_i \le 10\,\mathrm{MeV})$$
$$j = \mathrm{Ca, Si, O, Mg, Cl, Fe, H, C} \ldots, \tag{2}$$

where B_j is the pure characteristic gamma-ray spectrum of element j, and A_j the proportion of element j in I_{E_i}.

In practical applications, the parameters, θ_j, m, σ, t, j, and ε, are constants for a fixed setup and fixed element. Combining Eqs. (1) and (2), we obtained the following results:

$$B_j = a_j \left(\frac{N_A \theta_j}{m_j} \right) \sigma \varphi t j \varepsilon \quad j = \mathrm{Ca, Si, O, Mg, Cl, Fe, H, C} \ldots \tag{3}$$

$$w_j = k_j A_j \quad j = \mathrm{Ca, Si, O, Mg, Cl, Fe, H, C} \ldots, \tag{4}$$

where a_j and k_j are constants that can be calculated experimentally. For a fixed PGNAA analyzer, B is the spectrum library and a known variable. A_j can be calculated using I_{E_i} via the least-squares regression method.

The Monte Carlo simulation [15–17] model of PGNAA analyzer model DF-5701 is shown in Fig. 1a. Two 20 μg ^{252}Cf neutron sources were placed in the source chamber. Two 5″ × 5″NaI(Tl) scintillator detectors were used as the prompt gamma-ray detectors. The height of the analyzer belt gallery was 31 cm. The analyzer was suitable for a 1-m-wide belt. The simulated cement raw material load (belt material load per meter) was 100 kg/m, and the material thickness was 20.75 cm.

The main content of the sinter was iron oxide, which constituted more than 75% of the total material in weight. Iron oxide is a good gamma-ray shielding material; therefore, the gamma-ray energy spectrum of the sinter mixture exhibits self-absorption [18–21]. To quantify the self-absorption of gamma rays, a gamma-ray attenuation detection device was added after the PGNAA device. The system diagram is shown in Fig. 1b. A ^{137}Cs radioactive source was installed under the belt, and a Φ 2″ × 2″NaI(Tl) scintillator detector was installed above the material to detect the gamma-ray intensity.

The formula for gamma-ray self-absorption compensation is as follows [22]:

$$I_{0E_i} = I_{E_i} \exp \left(\frac{-\mu_{mE_i}}{\mu_0} k \ln \left(\frac{N}{N_0} \right) \right)$$
$$(1\,\mathrm{MeV} \le E_i \le 10\,\mathrm{MeV}), \tag{5}$$

where I_{0E_i} is the initial energy intensity without attenuation, I_{E_i} the energy intensity obtained by the PGNAA detector, μ_{mEi} the characteristic gamma-ray mass attenuation coefficient with energy E_i, N the count rate of the NaI(Tl) detector when a material exists on the belt, N_0 the
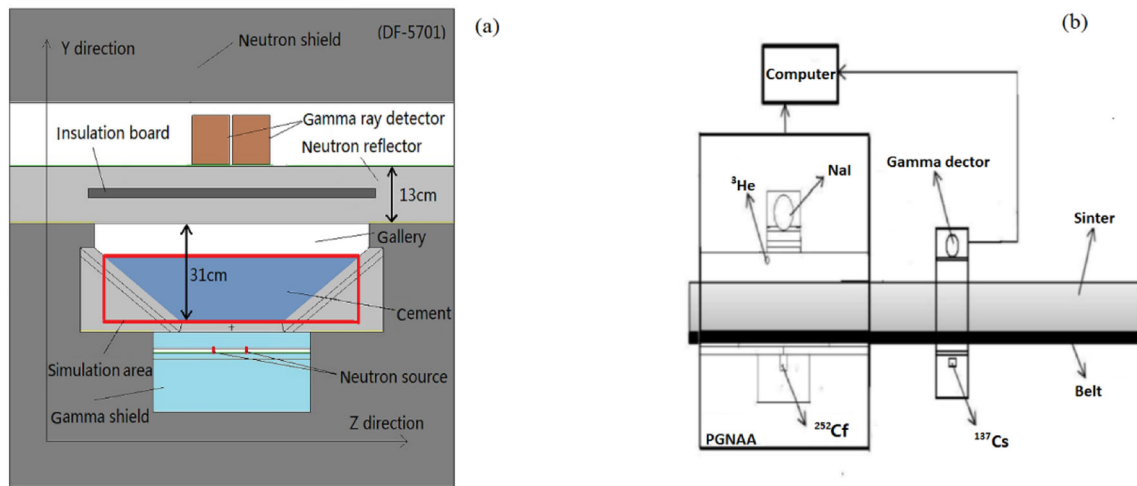
Fig. 1 (Color online) Experimental model. **a** DF-5701 simulation model **b** system structure diagram

count rate of the NaI(Tl) detector with no material on the belt, μ_0 the mass attenuation coefficient of gamma rays with an energy of 0.662 MeV, and k the correction factor.

The linear absorption coefficient μ of the material is defined as follows:

$$\mu = \sum N_i \sigma_i^{\gamma} \quad i = \text{Ca, Si, O, Mg, Cl, Fe, H, C} \ldots, \tag{6}$$

where N_i is the atomic density of each element, and σ_i^{γ} the total microscopic photon atomic cross section.

The formula to calculate N_{element} is as follows:

$$N_{\text{element}} = \frac{m_\rho}{\sum M_i f_i} f_{\text{element}} \times N_A \times 10^{-24}$$
$$i = \text{Ca, Si, O, Mg, Cl, Fe,} \tag{7}$$

where m_ρ is the mass density of the material being measured, M_i the atomic weight of each element, f_i the material proportion of each element, f_{element} the material proportion of the current element, and N_A the Avogadro constant. Based on the composition of the sinter mixture, $\frac{-\mu_{mE_i}}{\mu_0}$ can be calculated using Eqs. (6) and (7). As the count rate with material on the belt N, the count rate with no material on the belt N_0 and PGNAA energy intensity I_{E_i} can be obtained experimentally, the initial energy intensity I_{0E_i} can be calculated using Eq. (5).

3 Experiments

3.1 Monte Carlo calculations

The main oxides and components of the cement raw material and sintered mixture are shown in Table 1. The thermal neutron capture cross sections of Ca, Si, Fe, and Al are shown in Table 2. According to Tables 1 and 2, the comprehensive thermal neutron capture cross section of the

sinter mixture is 5.5 times that of the raw cement, indicating that the sinter mixture with the same load will consume more thermal neutrons than raw cement. Therefore, the detection device of the cement analyzer cannot directly detect the sinter mixture, and the device must be re-optimized.

The probability that the detector records the gamma ray emitted from position A is defined as the spatial gamma detection probability (SGDP) of position A. Furthermore, the spatial comprehensive detection probability (SCDP) at position A is defined as the product of the spatial thermal neutron distribution probability and spatial gamma detection probability at position A. Using the FMESH tally card [23] of MCNP, the spatial thermo neutron distribution probability (STNDP) and spatial fast neutron distribution probability (SFNDP) of the simulation area can be simulated easily. GTFADE is a Monte Carlo simulation software custom designed for simulating the SGDP. Using the GTFADE, the SGDP of the simulation area can be simulated easily.

The Monte Carlo simulation models are shown in Fig. 2. In the model, the X-direction is vertical to the paper surface, representing the belt running direction and the length of the test sample; the Y-direction represents the height of the analyzer and the thickness of the test sample; and the Z-direction represents the width of the analyzer and the sample. A cuboid with a length, width, and height of 90, 80, and 15 cm, respectively, was set as the simulation area. The simulation area was evenly divided into $90 \times 80 \times 15 = 108{,}000$ small lattice cells, and the SGDP, STNDP, and SFNDP were simulated. Two ^{252}Cf spontaneous fission neutron sources were used in the model under the test material. The energy distribution of neutrons can be approximated as a Watt distribution [24]. The average neutron energy of the source was approximately

Table 1 Oxide composition and content of cement raw material and sinter mixture

Oxide	CaO (%)	Al_2O_3 (%)	SiO_2 (%)	Fe_2O_3 (%)
Raw cement (dry-basis wt%)	44	3	13	2.5
Sinter mixture (loss-free wt%)	12	2	6	77

Loss-Free no loss basis

Table 2 Thermal neutron capture cross-section data of four elements

Element	Ca	Al	Si	Fe
Thermal neutron capture cross section (barns)	0.431	0.231	0.172	2.56

3.5 MeV, and the distance between the two sources was 18 cm.

Figure 2a shows the initial model (IM), which changes the test material from the cement raw material to the sinter mixture based on the DF-5701 model. The thickness of the sinter mixture was 15 cm. Because the density of the sinter mixture (1.9 tons per cubic meter) was greater than that of the cement raw material (1.3 tons per cubic meter), the height of the material gallery can be reduced. Figure 2b shows optimization model 1 (OM1), which reduced the height of the material gallery from 31 to 27.4 cm based on the IM. Figure 2c shows optimization model 2 (OM2), which reduced the height of the material gallery from 31 to 23.4 cm based on the IM. The neutron reflection plate in the model can enhance the STNDP of the detection area. Figure 2d shows optimization model 3 (OM3), which changed the material of the insulation board into high-density polyethylene (HDPE) based on OM2. Figure 2e shows optimization model 4 (OM4), which reduced the thickness of the neutron reflector from 13 to 10 cm based on OM4. According to Kamal Hadad et al. [19], HDPE is a good neutron-moderating material. Figure 2f shows optimization model 5 (OM5), which adds a 2-cm-thick HDPE [25, 26] above the gamma shield based on OM4 to enhance the neutron moderation ability of the model.

3.2 Experimental activities

In the experiment, the optimized device was used as the detection device, two 20 μg ^{252}Cf spontaneous fission neutron sources were used as the neutron excitation sources, and two sets of $\Phi\ 5'' \times 5''$ NaI(Tl) scintillator detectors were used as gamma-ray detectors.

Six groups of calibration samples were prepared in the experiment. The samples contained Fe_2O_3, SiO_2, CaO, MgO, Cl, and other components. The components of the calibration samples are listed in Table 3. To verify the adaptability of the model, nine groups of verification samples were prepared in the experiment, and the sample composition is shown in Table 4.

The cement raw material and sinter mixture were used to perform different load experiments. The experimental results of the cement raw material are shown in Fig. 3a. The analytical coefficient of iron A_{Fe} increased linearly with the belt load, demonstrating that the gamma-ray self-absorption of the cement as a raw material was weak. The experimental results for the sinter mixture are shown in Fig. 3b. The analytical coefficient of iron element A_{Fe} exhibited a quadratic curve relationship with an increase in the belt load, and the curve exhibited a turning point, which indicates the strong gamma-ray self-absorption of the sinter mixture. Therefore, a compensation correction operation was required. As shown in Fig. 3b, the sinter mixture load exhibited an approximately linear relationship in the range of 60–130 kg/m. The belt load directly affected the detection precision of each component in the experiment. The belt load must be in the linear region and should be as large as possible to increase the effective counting rate of the energy spectrum and improve the precision of the analysis results. In this experiment, 110 kg/m was selected as the experimental belt load.

Figure 4a shows the PGNAA energy spectrum of the raw cement meal. As shown from the figure, the characteristic peaks of Ca and Si were significant and no superposition interference of other elemental characteristic peaks occurred. In such an ideal energy spectrum, the contents of CaO and SiO_2 can be calculated directly from the characteristic peak areas of Ca and Si. Figure 4b shows the PGNAA energy spectrum of the sinter mixture. As shown, the characteristic peaks of Fe were ubiquitous in the energy spectrum, and the characteristic peaks of Ca and Si were suppressed by the characteristic peaks of iron and its Compton plateau. Therefore, the component contents of CaO and SiO_2 with peak areas could not be calculated in such an energy spectrum. The spectral library least-squares method was used in the experiment to accurately deconvolute the energy spectrum. The spectrum library, which contains the characteristic energy spectra of calcium, silicon, iron, aluminum, magnesium, chlorine, sulfur, sodium, and background, was established prior to the experiment. Through the least-squares operation, we can obtain the
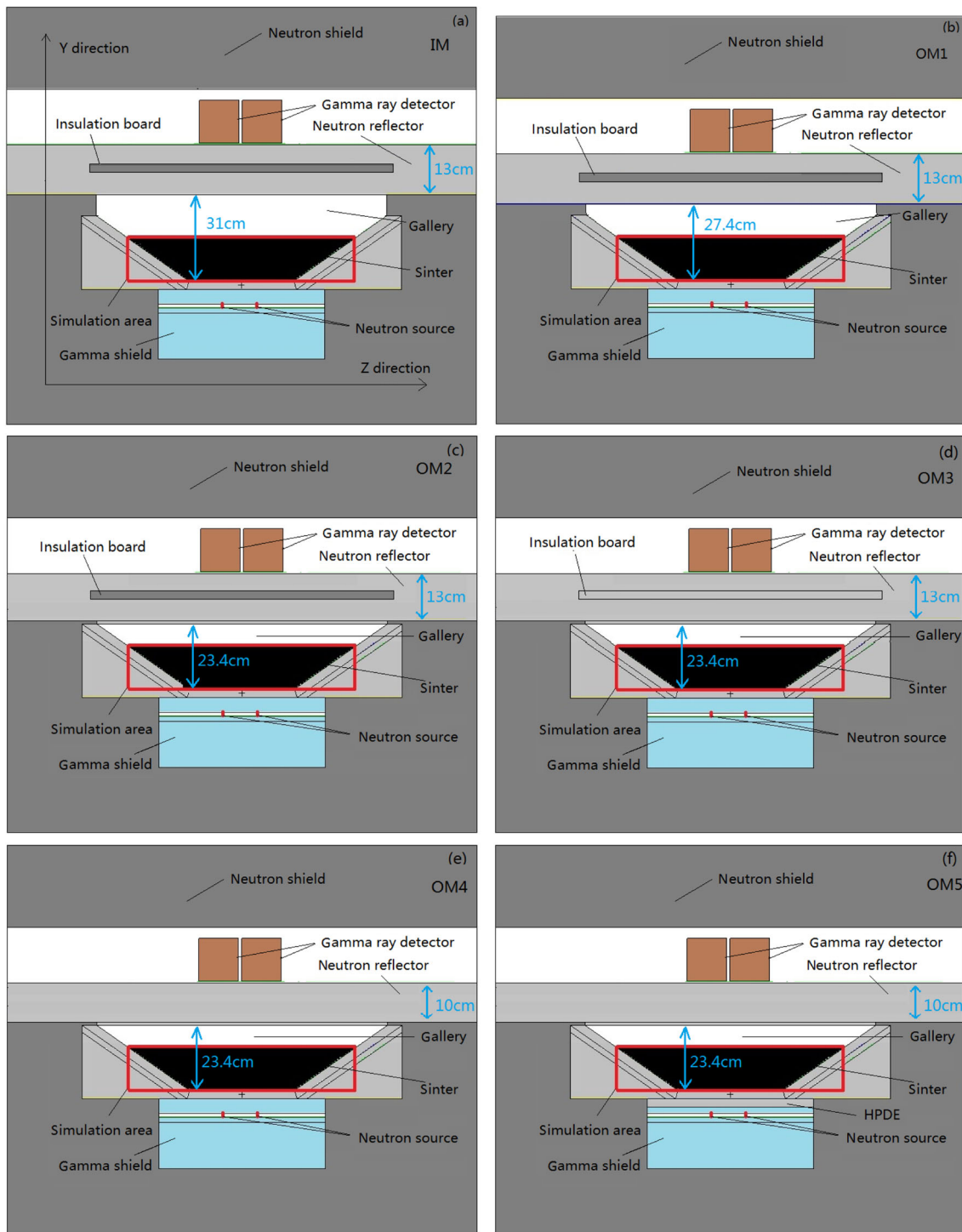
Fig. 2 (Color online) Monte Carlo simulation model. **a** IM **b** OM1 **c** OM2 **d** OM3 **e** OM4 **f** OM5

contribution of each element in the total spectrum, which corresponds to the content of related elements.

Six groups of calibration samples and nine groups of verification samples were placed in the PGNAA detection area to obtain the energy spectrum, and the energy spectrum collection time was 60 min. Subsequently, the samples were placed into the gamma attenuation detection area successively, and the corresponding the count rate with material on the belt N, the count rate with no material on the belt N_0 were recorded.

Table 3 Chemical composition of calibration samples (loss-free wt%)

Sample	TFe	SiO₂	CaO	MgO	Cl	Other
1-1#	46.34 ± 0.16	9.19 ± 0.08	9.8 ± 0.07	4.98 ± 0.1	1.22 ± 0.09	8.61
1-2#	48.23 ± 0.16	9.88 ± 0.08	9.92 ± 0.07	1.95 ± 0.08	0.94 ± 0.07	8.41
1-3#	50.75 ± 0.16	8.34 ± 0.08	8.14 ± 0.06	2.62 ± 0.08	0.51 ± 0.04	7.89
1-4#	54.6 ± 0.16	6.45 ± 0.08	6.73 ± 0.06	1.45 ± 0.08	0.27 ± 0.02	7.1
1-5#	52.85 ± 0.16	6.89 ± 0.08	5.54 ± 0.06	3.36 ± 0.08	0.69 ± 0.05	8.02
1-6#	58.1 ± 0.16	4.14 ± 0.06	4.53 ± 0.06	0.51 ± 0.07	0.33 ± 0.03	7.49

TFe total ferrous content

Table 4 Chemical composition of verification samples (loss-free wt%)

Sample	TFe	SiO₂	CaO	MgO	Cl	Other
2-1#	47.29 ± 0.16	9.54 ± 0.08	9.86 ± 0.07	3.47 ± 0.08	1.08 ± 0.08	8.49
2-2#	49.49 ± 0.16	9.11 ± 0.08	9.03 ± 0.07	2.29 ± 0.08	0.73 ± 0.05	8.14
2-3#	50.54 ± 0.16	8.39 ± 0.08	7.73 ± 0.06	2.66 ± 0.08	0.82 ± 0.06	8.2
2-4#	52.68 ± 0.16	7.4 ± 0.08	7.44 ± 0.06	2.04 ± 0.08	0.39 ± 0.03	7.47
2-5#	48.55 ± 0.16	8.77 ± 0.08	8.97 ± 0.07	3.8 ± 0.1	0.87 ± 0.06	8.23
2-6#	51.8 ± 0.16	7.62 ± 0.08	6.84 ± 0.06	2.99 ± 0.08	0.6 ± 0.04	7.95
2-7#	55.48 ± 0.16	5.52 ± 0.06	5.04 ± 0.06	1.94 ± 0.08	0.51 ± 0.04	7.73
2-8#	53.73 ± 0.16	6.67 ± 0.08	6.14 ± 0.06	2.41 ± 0.08	0.48 ± 0.04	7.54
2-9#	56.35 ± 0.16	5.3 ± 0.06	5.63 ± 0.06	0.98 ± 0.07	0.3 ± 0.02	7.29

Fig. 3 Change curves of belt load. **a** Change curve of cement raw material load **b** change curve of sinter mixture load
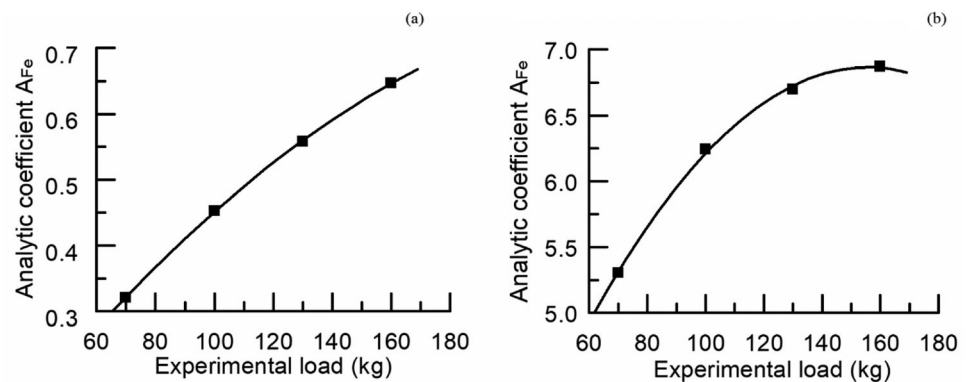
Fig. 4 PGNAA spectrum **a** PGNAA spectrum of cement raw material **b** PGNAA spectrum of sinter mixture
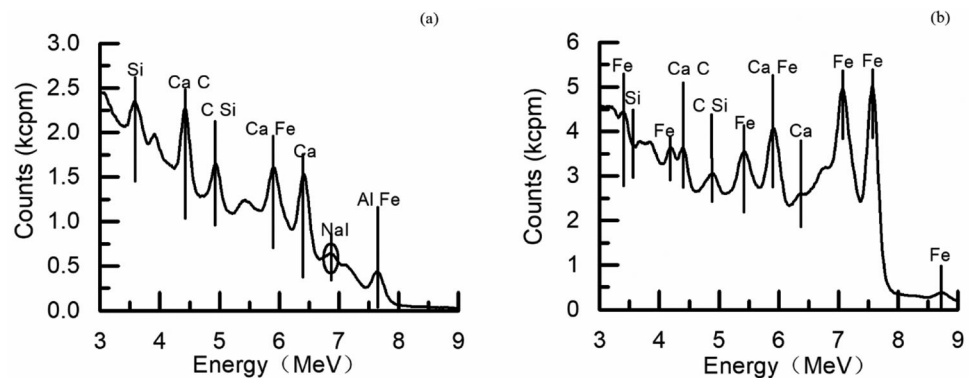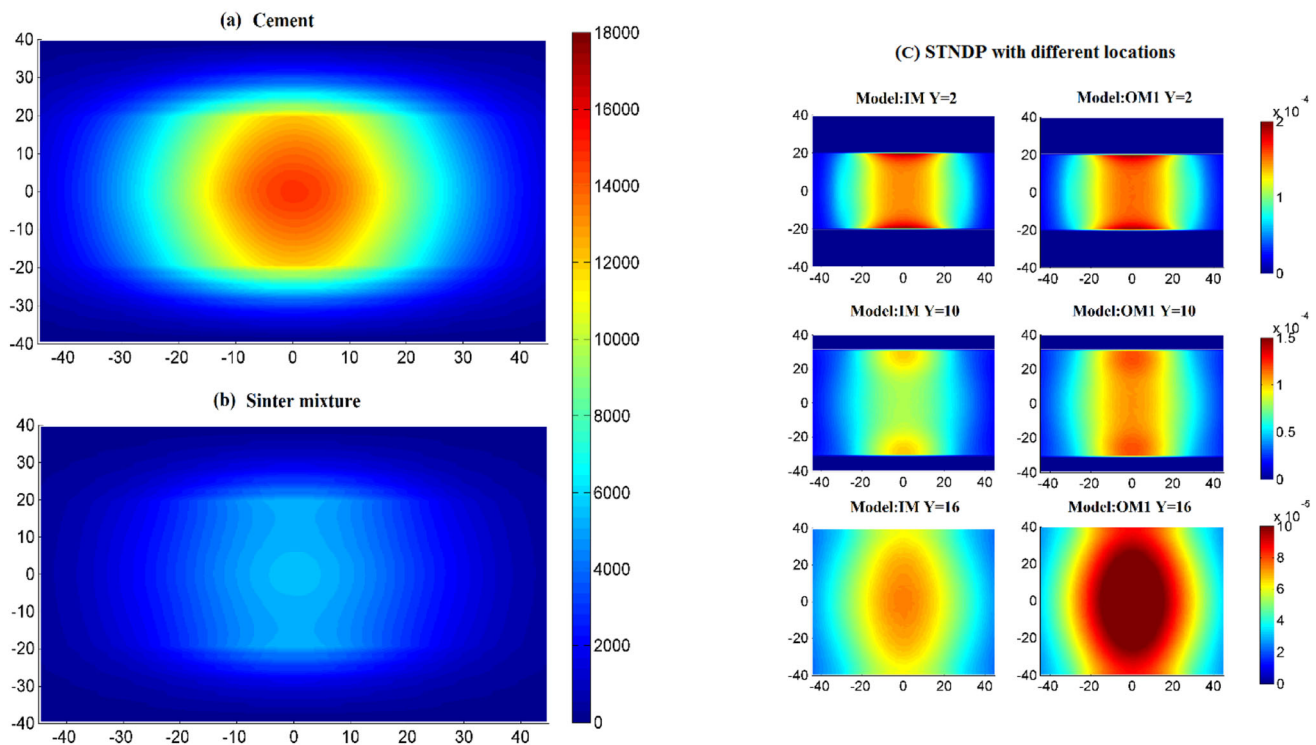
Fig. 5 (Color online) SCDP of different test materials and STNDP with different locations. **a** SCDP of DF-5701 model when test material is cement raw material. **b** SCDP of DF-5701 model when test material is sinter mixture. **c** STNDP with different locations (IM vs. OM1)

Table 5 Different locations of STNDP data

Material thickness coordinate	$Y = 2$	$Y = 10$	$Y = 16$
STNDP of IM	1.2725	0.7511	0.5575
STNDP of OM1	1.2779	0.8122	0.7612

4 Results and discussion

4.1 Monte Carlo calculation result

The simulation requirements included the neutron source following Watt distribution, a cross-section database of ENDF/B-VI [27], F4 cell flux tally, and FMESH card. A total of 1×10^9 initial particles were used for better simulation statistics.

Different test materials of the same simulation model will exhibit different SCDPs because the test material is a neutron-moderating material. Figure 5a, b shows the SCDP simulation results for different test materials based on the DF-5701 model. The test material shown in Fig. 5a is cement raw material, and the test material shown in Fig. 5b is the sinter mixture. In the figure, the abscissa and ordinate represent the material length and width, respectively. As shown, the SCDP of cement is significantly higher than that

of the sinter mixture. This is because the main element in the sinter mixture is iron, and its neutron-moderation ability is significantly less than those of light elements such as calcium and silicon; furthermore, the STNDP of cement is higher than that of the sinter mixture for the same neutron source. Table 2 shows that the thermal neutron absorption cross section of iron is much higher than that of calcium. Compared with the raw cement material, the sinter mixture consumed more thermal neutrons; therefore, the STNDP of the sinter mixture is much lower than that of the cement raw material.

As shown in Fig. 5c and Table 5, the STNDP of OM1 increased by 36.54% at the top of the material but almost no increase was observed at the bottom near the radioactive source. As the height of the gallery decreased, the neutron reflection ability of the device improved; consequently, the thermal neutron flux on the upper part of the material increased. It can be inferred from Fig. 5c that the effective approach to improve the SCDP of the system is to reduce the height of the material gallery; however, this is restricted. The passing capacity caused by the change in material shape must be ensured when the belt is operating.

Figure 6a shows the distribution curves of the STNDP, SGDP, and SCDP with the material thickness in the DF-5701 model. The abscissa in the figure is the y-axis coordinate of the model, which represents the thickness change
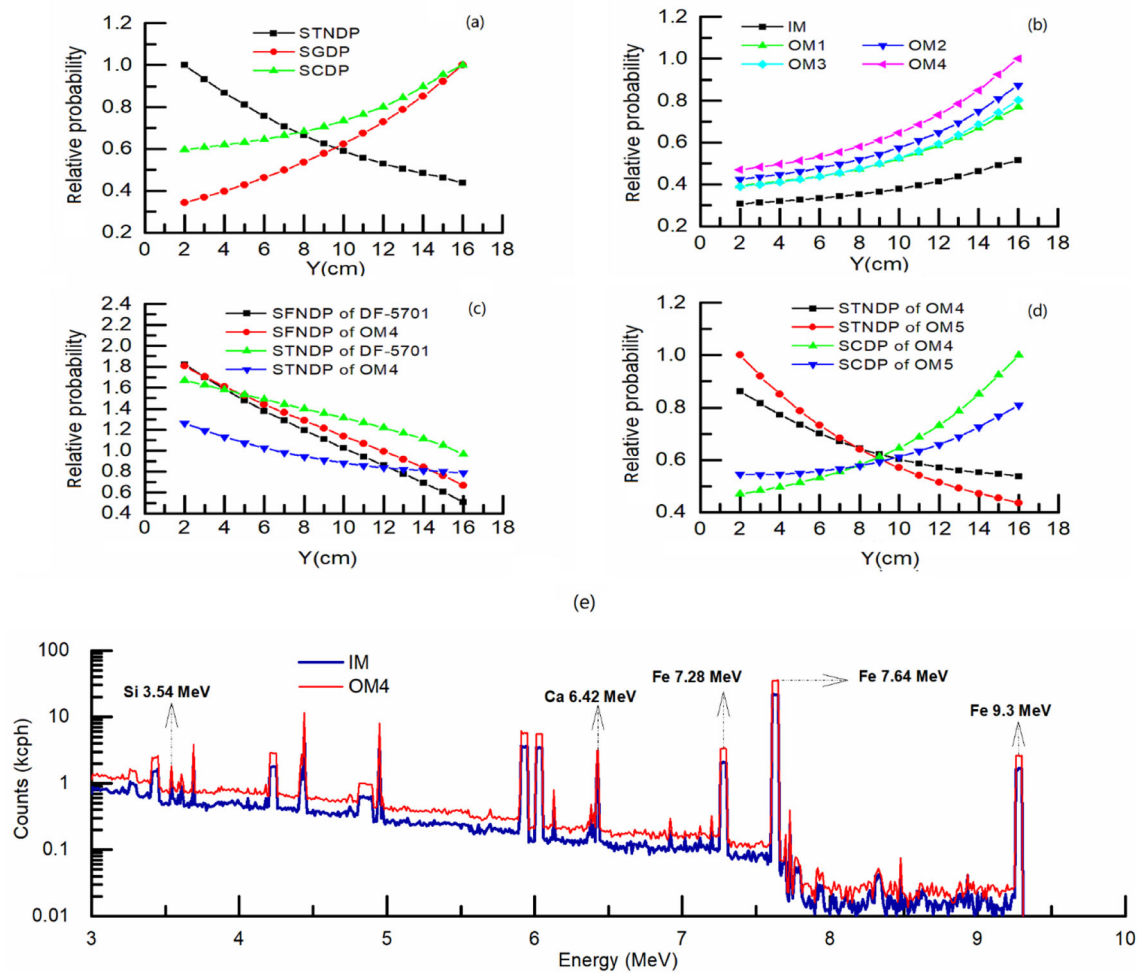
Fig. 6 (Color online) Simulation result curves. **a** Different detection efficiency curves of model DF-5701. **b** SCDP curves of different models. **c** Fast and thermo neutron distribution curves. **d** STNDP and SCDP comparison curves. **e** Simulation energy spectrum of IM and OM4 model

of the material. As shown, the STNDP decreased with increasing material thickness, the SGDP increased with the material thickness, and the SCDP increased with the material thickness. A thicker material enabled the absorption of more neutrons and hence a reduced STNDP. At locations closer to the detector, the spatial detection angle is larger; therefore, the SGDP increases with the thickness of the material.

Figure 6b and Table 6 shows the total comprehensive detection efficiency of each simulation model. As shown in the figure and table, OM4 achieved the highest total comprehensive detection efficiency. Figure 6c shows a

comparison of the probability curves of fast neutron and thermal neutron distributions under two models: the DF-5701 model for cement material detection and OM4. As shown in the figure, the thermal neutron distribution probability of OM4 is lower than that of the cement model, whereas the fast neutron distribution probability is higher than that of the cement model, indicating that OM4 may exhibit problems in neutron moderation. To solve this problem, OM5 was designed. The comparison results of the OM5 and OM4 simulations are shown in Fig. 6d. As shown, the comprehensive detection efficiency of OM5 is

Table 6 Counts with different model data

Model	IM	OM1	OM2	OM3	OM4	OM5
Counts	9780	13513	14906	13672	16776	15938
Promotion	0	38.17%	52.41%	39.79%	71.52%	62.95%

Table 7 Experimental data of SiO$_2$ calibration samples

Sample	1-1#	1-2#	1-3#	1-4#	1-5#	1-6#
A_{Si}	0.135	0.134	0.118	0.084	0.102	0.044
N/N_0	0.582	0.501	0.528	0.479	0.608	0.452
A_{Si}^1	0.142	0.151	0.131	0.099	0.105	0.054
Laboratory content (wt%)	9.19	9.88	8.34	6.45	6.89	4.14
Initial calculate content (wt%)	9.39	9.33	8.38	6.36	7.43	3.99
Calculate content after correction (wt%)	9.14	9.67	8.5	6.62	6.97	3.98
Initial RMS error (wt%)			0.333			
RMS error after correction (wt%)			0.148			

A_{Si} Initial analytical coefficient of Si

A_{Si}^1: Analytical coefficient of Si after correction

Table 8 Experimental data of CaO calibration samples

Sample	1-1#	1-2#	1-3#	1-4#	1-5#	1-6#
A_{Ca}	0.265	0.253	0.207	0.168	0.162	0.103
N/N_0	0.582	0.501	0.528	0.479	0.608	0.452
A_{Ca}^1	0.291	0.298	0.239	0.206	0.173	0.132
Laboratory content (wt%)	9.8	9.92	8.14	6.73	5.54	4.53
Initial calculate content (wt%)	10.02	9.59	7.94	6.55	6.34	4.23
Calculate content after correction (wt%)	9.74	9.97	7.98	6.86	5.75	4.36
Initial RMS error (wt%)			0.398			
RMS error after correction (wt%)			0.143			

A_{Ca}: Initial analytical coefficient of Ca

A_{Ca}^1: Analytical coefficient of Ca after correction

Table 9 Experimental data of CaO of verification samples

Sample	2-1#	2-2#	2-3#	2-4#	2-5#	2-6#	2-7#	2-8#	2-9#
Laboratory content %	9.86	9.03	7.73	7.44	8.97	6.84	5.04	6.14	5.63
Calculate content %	9.97	9.30	7.84	7.37	9.16	6.96	4.90	6.09	5.44
RMS error (wt%)					0.152				

lower than that of OM4, and that OM4 is the best detection model for this simulation calculation.

Figure 6d shows that the probability of thermal neutron distribution at the bottom of the material in the OM5 model improved, but the probability of thermal neutron distribution at the top of the material decreased, and the comprehensive detection efficiency of the OM5 model decreased as well. This indicates that the sinter mixture possessed sufficient moderation ability for the fast neutrons emitted by the ^{252}Cf neutron source, and no additional moderation materials were required. However, the neutron moderation ability of cement, coal, bauxite, and other bulk materials was higher than that of the sinter mixture. Therefore, when using PGNAA technology to detect these materials, no additional moderation materials are required.

The MCNP code was used to simulate the characteristic gamma spectrum of the IM and OM4 models. A comparison diagram of the energy spectrum is shown in Fig. 6e. It is evident that the characteristic peak counts of Fe, Ca, and Si in the characteristic energy spectrum of the OM4 model improved significantly.

4.2 Measurement experiment result

Table 7 shows the experimental data of the SiO$_2$ calibration samples. It includes the results of the chemical element test by the sampling method in the laboratory, the online results obtained using the library least-squares methods in PGNAA, and the results corrected by self-absorption. Table 8 shows the experimental data of the CaO
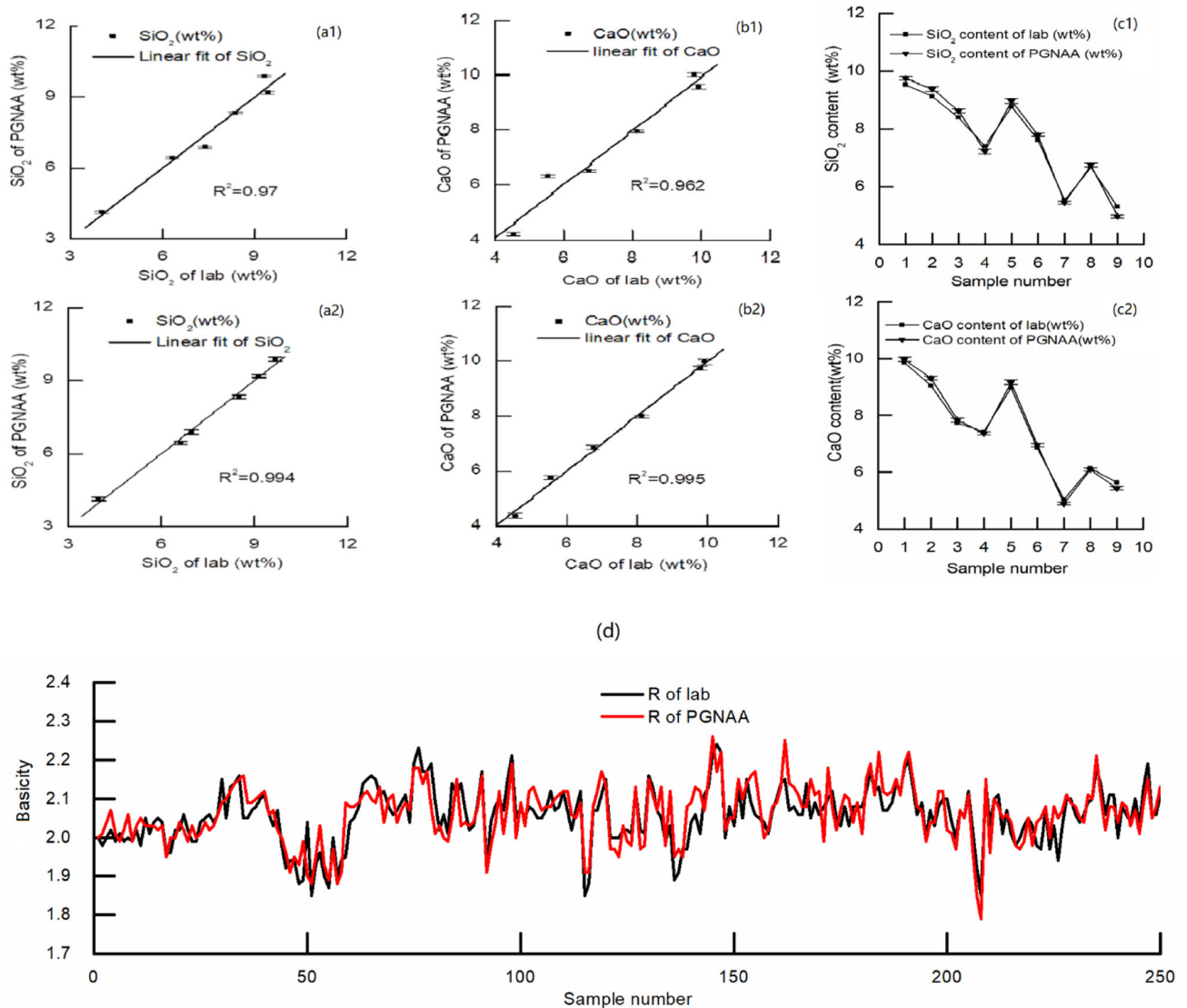
Fig. 7 (Color online) Curves of measurement experiment. **a1** Calibration curve of silicon dioxide before gamma self-absorption correction. **a2** Calibration curve of silicon dioxide after gamma self-absorption correction. **b1** Calibration curve of calcium oxide before gamma self-absorption correction. **b2** Calibration curve of calcium oxide after gamma self-absorption correction. **c1** SiO_2 comparison curve of verification samples **c2** CaO comparison curve of verification samples. **d** Basicity contrast curve

Table 10 Experimental data of SiO_2 verification samples

Sample	2-1#	2-2#	2-3#	2-4#	2-5#	2-6#	2-7#	2-8#	2-9#
Laboratory content %	9.54	9.11	8.39	7.4	8.77	7.62	5.52	6.67	5.3
Calculate content %	9.73	9.38	8.62	7.21	8.97	7.79	5.45	6.74	4.98
RMS error (wt%)					0.205				

Table 11 Error data of PGNAA analyzer in sintering plant

Item	CaO	SiO_2	Basicity
Range	12%–15%	6%–7.2%	1.85–2.24
RMS error (1σ)	0.25%	0.10%	0.04

calibration samples. Table 10 shows the experimental data of the SiO_2 verification samples. Table 9 shows the experimental data of the CaO verification samples. Figure 7a1, a2 shows the calibration curves of SiO_2. Figure 7b1, b2 shows the calibration curves of CaO. Figure 7c1 shows the SiO_2 comparison curve of the verification samples. Figure 7c2 shows the CaO comparison

Table 12 Production data before and after using the analyzer

Data	TFe	R	FeO	SiO_2	CaO	FCPR (%)	BSR (%)
Jan–Jul average	54.19	2.10	8.83	6.62	13.90	84.38	84.33
Aug	54.35	2.058	8.98	6.57	13.5	89.26	89.01
Sep	54.58	2.065	9.05	6.54	13.47	86.41	87.25
Oct	54.24	2.093	9.04	6.54	13.69	89.06	87.77
Nov	54.12	2.075	9.20	6.70	13.90	91.36	89.19
Aug–Nov average	54.32	2.07	9.07	6.59	13.64	89.02	88.31
Promotion value						4.64	3.98

curve of the verification samples. After the gamma-ray self-absorption correction, the calibration RMS error of SiO_2 increased from 0.333 to 0.148% (Table 7), and the linear correlation coefficient R^2 improved from 0.970 to 0.994 (Fig. 7a1, a2). Meanwhile, the calibration RMS error of CaO increased from 0.398 to 0.143% (Table 8), and the linear correlation coefficient R^2 improved from 0.962 to 0.995 (Fig. 7b1, b2). The CaO and SiO_2 RMS errors of the nine groups of verification samples were 0.152% and 0.205% (Tables 9 and 10), respectively.

4.3 Application effect of analyzer

The improved analyzer was applied in a sintering plant and installed in the second mixing process point of the sintering batching workshop. The analyzer installation point was approximately 15 min behind the batching belt; however, it was approximately 4 h and 45 min ahead of the original control method.

In the actual sintering production process, the composition of each element changes slightly. By substituting the content of each element detected by the analyzer as a variable into the calculation formula, the dynamic detection μ_{mEi} curve can be realized, and the accuracy of the correction model improved. A comparison of the basicity data curves obtained using the analyzer and experimentally is shown in Fig. 7d. It is clear that the basicity trend obtained using the PGNAA analyzer was consistent with that from performing a chemical test in the laboratory. The error data are shown in Table 11. The standard error of basicity was only 0.04, indicating the excellent accuracy of the PGNAA analyzer in detecting the basicity index of the sinter mixture. In August 2017, the sintering plant began using the analyzer to guide batching production. After the analyzer was used, the basicity stability rate (BSR) of the sintering plant improved by 3.98%, and the first-class product rate (FCPR) of the sinter improved by 4.64%. The factory production data are shown in Table 12.

5 Conclusion

In the experiment, the DF-5701 neutron activation analyzer was re-optimized, and the height of the material corridor was reduced from 31 to 23.4 cm. Thermal insulation materials were replaced with HDPE, and the thickness of the neutron reflector was reduced from 13 to 10 cm. The distance between the measured material and the detector was reduced from 43 to 32.4 cm, which effectively increased the comprehensive detection efficiency of the detection area. The comprehensive detection efficiency of the optimized model increased by 71.52%.

In the neutron activation analysis of the sinter mixture, the gamma self-absorption effect was prominent. In the experiment, the gamma-ray self-attenuation degree detection device was installed behind the PGNAA analyzer. The energy spectrum was corrected by substituting the theoretical calculation parameter $\frac{-\mu_{mE_i}}{\mu_0}$, the count rate with material on the belt N, the count rate with no material on the belt N_0, and the energy spectrum I_{E_i} into Eq. (5). By gamma-ray self-absorption correction, the calibration RMS error of SiO_2 improved from 0.333 to 0.148%, and the R^2 improved from 0.970 to 0.994. The calibration RMS error of CaO increased from 0.398 to 0.143%, and the R^2 improved from 0.962 to 0.995. The improved analyzer was applied in a sintering plant to guide batching production. After the analyzer was applied, the BSR of the sintering plant improved by 3.98%, and the FCPR of the sinter improved by 4.64%.

References

1. J.B. Yang, X.G. Tuo, Z. Li et al., Mc simulation of a PGNAA system for on-line cement analysis. Nucl. Sci. Tech. **21**, 221–226 (2010). https://doi.org/10.13538/j.1001-8042/nst.21.221-226

2. F. Zhang, J.T. Liu, Monte Carlo simulation of PGNAA system for determining element content in the rock sample. Radioanal. Nucl. Chem. **299**, 1219–1224 (2014). https://doi.org/10.1007/s10967-013-2858-3

3. R. Khelifi, A. Amokrane, P. Bode, Detection limits of pollutants in water for PGNAA using Am–Be source. Nucl. Inst Methods Phys. Res. B **262**(2), 329–332 (2007). https://doi.org/10.1016/j.nimb.2007.06.003

4. W.A. Metwally, R.P. Gardner, C.W. Mayo, Elemental PGNAA analysis using gamma-gamma coincidence counting with the library least-squares approach. Nucl. Instrum. Methods Phys. Res. **213**, 394–399 (2004). https://doi.org/10.1016/S0168-583X(03)01660-4

5. M. Borsaru, M. Berry, M. Biggs et al., In situ determination of sulphur in coal seams and overburden rock by PGNAA. Nucl. Instrum. Methods Phys. Res. **213**, 530–534 (2004). https://doi.org/10.1016/S0168-583X(03)01623-9

6. M. Borsaru, C. Smith, J. Merritt et al., In situ determination of salinity by PGNAA. Appl. Radiat. Isot. **64**, 630–637 (2006). https://doi.org/10.1016/j.apradiso.2005.12.015

7. C. Oliveira, J. Salgado, I.F. Goncalves et al., A Mente Carlo study of the influence of the geometry arrangements and structural materials on a PGNAA system performance for cement raw material analysis. Appl. Radiat. Isot. **48**, 1349–1354 (1997). https://doi.org/10.1016/s0969-8043(97)00130-9

8. A.A. Naqvi, M.M. Nagadi, Performance comparison of an ^{241}Am–Be neutron source-based pgnaa setup with the KFUPM PGNAA setup. Radioanal. Nucl. Chem. **260**, 641–646 (2004). https://doi.org/10.1023/b:jrnc.0000028225.07280.74

9. A.A. Naqvi, A Monte Carlo comparison of PGNAA system performance using ^{252}Cf neutrons, 2.8-MeV neutrons and 14-MeV neutrons. Nucl. Instrum. Methods A **511**, 400–407 (2003). https://doi.org/10.1016/s0168-9002(03)01949-1

10. C. Oliveira, J. Salgado, F. Leitao, Density and water content corrections in the gamma count rate of a PGNAA system for cement raw material analysis using the MCNP Code. Appl. Radiat. Isot. **49**, 923–930 (1998). https://doi.org/10.1016/s0969-8043(97)10111-7

11. J.G. Fantidis, G.E. Nicolaou, C. Potolias et al., The comparison of four neutron sources for Prompt Gamma Neutron Activation Analysis (PGNAA) in vivo detections of boron. J. Radioanal. Nucl. Chem. **290**, 289–295 (2011). https://doi.org/10.1007/s10967-011-1315-4

12. S.L. Wu, G.J. Wang, W.Z. Jiang et al., Interaction between lump ore and sinter in BF. Iron Steel **42**(3), 10–13 (2007). https://doi.org/10.3321/j.issn:0449-749X.2007.03.003

13. F. Shi, J. Ma, J. Zhao et al., Detection sensitivities of C and O in coal due to a channel in the moderator. Radiat. Meas. **46**(1), 88–91 (2011). https://doi.org/10.1016/j.radmeas.2010.08.025

14. R.P. Gardner, C.W. Mayo, NaI detector nonlinearity for PGNAA applications. Appl. Radiat. Isot. **51**(2), 189–195 (1999). https://doi.org/10.1016/S0969-8043(98)00183-3

15. Y. Xiao, Q.X. Zhang, Monte Carlo simulation of the influence of medical foam on particle dose. Nucl. Tech. **43**(9), 090302 (2020). https://doi.org/10.11889/j.0253-3219.2020.hjs.43.090302. **(in Chinese)**

16. L. Ma, L.C. Tian, Y.Y. Ma et al., Research on optimal design of new neutron detector based on 6Li + CdTe. Nucl. Tech. **43**(8), 080401 (2020). https://doi.org/10.11889/j.0253-3219.2020.hjs.43.080401. **(in Chinese)**

17. J.C. Ren, K. Xu, M.Y. Ye et al., Study on the application of GEANT4 for CFETR neutronics analyses. Nucl. Tech. **43**(3), 030604 (2020). https://doi.org/10.11889/j.0253-3219.2020.hjs.43.030604. **(in Chinese)**

18. C. Cheng, W.B. Jia, D.Q. Hei et al., Study of influence of neutron field and γ-ray self-absorption on PGNAA measurement. Atom. Energy Sci. Technol. **48**, 802–806 (2014). https://doi.org/10.7538/yzk.2014.48.S0.0802. **(in Chinese)**

19. M.E. Medhat, Gamma-ray attenuation coefficients of some building materials available in Egypt. Ann. Nucl. Energy **36**, 849–852 (2009). https://doi.org/10.1016/j.anucene.2009.02.006

20. L.T. Yang, C.F. Chen, X.X. Jin et al., Research on accurate calculation method of γ-ray self-absorption correction factor. Atom. Energy Sci. Technol. **51**, 323–329 (2017). https://doi.org/10.7538/yzk.2017.51.02.0323. **(in Chinese)**

21. P.C. Liu, Q.Y. Liu, Z.J. Ma et al., Design of gas bremsstrahlung absorber at high energy photon source beamlines. Nucl. Tech. **43**(9), 090102 (2020). https://doi.org/10.11889/j.0253-3219.2020.hjs.43.090102. **(in Chinese)**

22. L. Zhao, X. Xu, J.B. Lu et al., Study on element detection and its correction in iron ore concentrate based on a prompt gamma-neutron activation analysis system. Nucl. Sci. Tech. **30**, 58 (2019). https://doi.org/10.1007/s41365-019-0579-1

23. A.L Swift, E.A. McKigney, R.C. Schirato et al., A Verification of MCNP6 FMESH Tally Capabilities (2015)

24. K. Hadad, M. Nematollahi, H. Sadeghpour et al., Moderation and shielding optimization for a 252Cf based prompt gamma neutron activation analyzer system. Int. J. Hydrog. Energy **41**(17), 7221–7226 (2016). https://doi.org/10.1016/j.ijhydene.2015.12.20820

25. K.S. Mann, M.S. Heer, A. Rani, Effect of low-Z absorber's thickness on gamma-ray shielding parameters. Nucl. Instrum. Methods Phys. Res. **797**, 19–28 (2015). https://doi.org/10.1016/j.nima.2015.06.013

26. Y. Gong, X.C. Guan, Q. Wang et al., Design of moderator for boron neutron capture therapy based on D–D neutron source. Nucl. Tech. **43**(9), 090303 (2020). https://doi.org/10.11889/j.0253-3219.2020.hjs.43.090303. **(in Chinese)**

27. Team M C, Book MCNP—A General Monte Carlo N-Particle Transport Code, Version 5,Appendix G—MCNP Data Libraries